



# Simulation of Shale Gas Transport and Production with Complex Fractures using Embedded Discrete Fracture Model

Wei Yu<sup>a</sup> , Yifei Xu<sup>b</sup>, Malin Liu<sup>c\*</sup>, Kan Wu<sup>a</sup> , Kamy Sepehrnoori<sup>b</sup>

<sup>a</sup>Dept. of Petroleum Engineering, Texas A&M University, College Station, TX 77845

<sup>b</sup>Dept. of Petroleum and Geosystems Engineering, The University of Texas at Austin, Austin, TX 78705

<sup>c</sup>Institute of Nuclear and New Energy Technology, Tsinghua University, Beijing, China

\*Corresponding author.

E-mail address: liumalin@mail.tsinghua.edu.cn

## Abstract

The goal of this study is to develop a new model to simulate gas and water transport in shale nanopores and complex fractures. We first derive a new gas diffusivity equation to consider multiple important physical mechanisms such as gas desorption, gas slippage and diffusion, and non-Darcy flow. For complex fractures, we implement a state-of-the-art embedded discrete fracture model (EDFM). We verify this numerical model against a commercial reservoir simulator for shale gas simulation with multiple planar fractures. After that, we perform a series of simulation studies to investigate the impacts of complex gas transport mechanisms and various fracture geometries on well performance. The critical parameters controlling well performance are identified. The simulation results reveal that modeling of gas production from complex fractures as well as modeling important gas transport mechanisms in shale gas reservoirs is extremely significant.

**Keywords:** shale nanopores, complex fractures, natural fractures, embedded discrete fracture model, heterogeneity

This article has been accepted for publication and undergone full peer review but has not been through the copyediting, typesetting, pagination and proofreading process which may lead to differences between this version and the Version of Record. Please cite this article as  
doi: 10.1002/aic.16060

© 2017 American Institute of Chemical Engineers (AIChE)

Received: Jul 20, 2017; Revised: Nov 17, 2017; Accepted: Dec 13, 2017

## Introduction

Gas shales are characterized by extremely low permeability (nanodarcies), low porosity (2-8%) and high total organic carbon (1-14%), which can be both source rock and reservoir rock.<sup>1</sup> In recent years, the economic viability of shale gas production has been enabled with the advances in hydraulic fracturing technologies and horizontal drilling. It has been estimated by U.S. Energy Information Administration (EIA) that shale gas production accounts for over 50% of total U.S. natural gas production in 2015.<sup>2</sup> Hence, shale gas has contributed significantly to the total natural gas supply in the U.S.

Gas transport in shale formation involves complex gas transport mechanisms due to the presence of a large amount of nanopores and organic matter, which include gas desorption, adsorbed gas porosity, gas slippage, and Knudsen diffusion etc.<sup>3-9</sup> Yu et al.<sup>9</sup> reported that the adsorbed gas porosity can be up to as high as 3.8% based on the experimental measurements of gas adsorption isotherm in some area of Marcellus shale. However, this important effect has not yet been well documented and clearly understood in the literature. Furthermore, complex fracture networks are commonly observed based on microseismic measurements<sup>10-11</sup> and fracture propagation models,<sup>12-15</sup> especially in the presence of pre-existing natural fractures. In addition, fracture width and conductivity vary along fracture length, which has been observed and predicted by both experimental studies and fracture models.<sup>14-17</sup> Moreover, the fracture conductivity is pressure-dependent, which decrease with the reservoir depletion due to proppant embedment.<sup>18-20</sup> Hence, the complex gas transport mechanisms and complex fracture geometries pose a great

challenge to accurately and efficiently evaluate and simulate well performance in shale gas reservoirs.

In recent years, considerable efforts have been made to model well performance from shale reservoirs with complex fracture geometry analytically and semi-analytically.<sup>21-27</sup> However, these analytical and semi-analytical approaches are difficult to fully capture the complex physics existed in shale gas reservoirs such as heterogeneity, multiphase flow (gas/water), pressure-dependent rock properties and fracture conductivity, disconnected natural fractures, and fractures with any orientation in 3D dimension, etc. In accordance, Cipolla et al.<sup>1</sup> stated that numerical reservoir simulation is the most rigorous method to model shale-gas reservoirs, which can incorporate the complex nature of fracture geometry and long-time transient gas flow behavior due to very low permeability of shale matrix. Regarding numerical methods with structured grid (single-porosity model), local grid refinement (LGR) is often used to model hydraulic fractures, where a small cell is placed for fracture and some cells with logarithmically increasing size are close to fracture.<sup>28-29</sup> However, this method is mainly limited to two simple fracture patterns such as bi-wing fractures and orthogonal fracture networks. Such fracture geometries are inadequate to represent the complex nature of fracture geometry in reality. Similarly, the traditional dual-continuum (dual-porosity or dual-permeability) numerical models<sup>30</sup> have the limitations for explicitly modeling complex fractures and cannot adequately account for anisotropy, heterogeneity, and fracture connectivity.<sup>31-32</sup>

With the recent advances in discrete fracture models using unstructured gridding with local refinement near the fractures, the true complex fracture geometry can be better modeled.<sup>33-35</sup>

However, the unstructured grids are still challenging to use efficiently in the field scale due to very complicated gridding issues and an expensive computational cost. Recently, a multi-segment well approach<sup>36-37</sup> has been developed to dynamically model hydraulic fractures. However, this approach is difficult to handle a large number of isolated natural fractures, which has no connection to primary hydraulic fractures and wellbore. In order to overcome the above issues, a state-of-the-art embedded discrete fracture model (EDFM) was developed to use for in-house simulator developments.<sup>38-45</sup> Recently, it has been widely extended to use in commercial reservoir simulators in a nonintrusive manner.<sup>32,46-50</sup> In EDFM, the complex fractures are embedded in conventional structured matrix grids explicitly without the need of LGR in the vicinity of fractures. This approach is simpler and faster to capture the complex fracture geometries. Accordingly, the EDFM approach is fully implemented in the model development of this study. More details will be discussed later in the text. Although there are many existing numerical models for shale gas simulation,<sup>51-55</sup> many of the above complex phenomenon have not been completely captured, and hence it is necessary to develop a powerful model to fill this gap in the petroleum industry.

In this study, we derive a new diffusivity equation by considering complex physics such as pore volume occupied by adsorbed gas, pressure-dependent rock properties, non-Darcy flow, and multiphase flow for describing gas transport and flow in shale formations. Furthermore, we fully implement the EDFM approach in the numerical model to efficiently simulate fluid flow behavior in the complex fracture geometries. In addition, we account for the natural fractures with multiple sets and the non-planar fractures with varying fracture width and conductivity across the fracture. The pressure-dependent fracture conductivity is included. The matrix and

fracture systems can have different sets of relative permeability curves. We verify the numerical model against a commercial reservoir simulator for simulation of gas and water flow in shale gas reservoirs with multiple planar fractures and non-Darcy flow and gas desorption effects. After verification, we perform a series of case studies to examine the impacts of various flow mechanisms discussed above, natural fractures, non-planar hydraulic fractures, pressure-dependent matrix permeability and fracture conductivity, and reservoir heterogeneity on well performance. The non-planar fracture geometry is predicted using a complex hydraulic fracture propagation model.

## Mass Conservation Equation

Two-phase flow (gas/water) are considered for deriving the mass conservation equations for simulation of shale gas production in this study. Each phase is present at equilibrium considering the viscous, gravity, and capillary forces. Gas and water can also be treated as two components. It is assumed that gas and water phases are independent without component interactions. The general mass conservation equation for component  $i$  ( $i = g$  for gas and  $i = w$  for water) can be written as

$$\frac{\partial W_i}{\partial t} + \vec{\nabla} \cdot \vec{F}_i - R_i = 0 \quad (1)$$

where  $W_i$ ,  $\vec{F}_i$ ,  $R_i$ , and  $t$  are the accumulation, flux, source, and time terms, respectively.<sup>56</sup> It should be mentioned that the unit of the above equation is lb-moles per unit bulk volume per unit time.

The accumulation term for gas component considering gas saturation, gas adsorption and pore volume occupied by adsorbed gas near the pore surface is expressed below:

$$W_g = \phi S_g (1 - c_{ag}) \xi_g + (1 - \phi) \rho_s v_{ag} \xi_{ag} \quad (2)$$

where  $\phi$  is porosity,  $S_g$  is gas saturation,  $c_{ag}$  is the volume fraction of adsorbed gas per unit pore volume,  $\xi_g$  is the molar density of gas phase,  $\rho_s$  is the rock density in ton per unit volume of solid,  $v_{ag}$  is the specific volume of gas adsorbed per unit mass of bulk rock (standard cubic feet per ton, scf/ton),  $\xi_{ag}$  is the molar density of adsorbed gas in lb-mole/ft<sup>3</sup>.

The accumulation term for water component without considering water adsorption is below:

$$W_w = \phi S_w \xi_w \quad (3)$$

where  $\xi_w$  is the molar density of water phase in lb-mole/ft<sup>3</sup> and  $S_w$  is water saturation.

The flux of gas and water components can be written as

$$\vec{F}_g = \xi_g \vec{u}_g \quad (4)$$

$$\vec{F}_w = \xi_w \vec{u}_w \quad (5)$$

where  $\vec{u}_g$  and  $\vec{u}_w$  represent the superficial velocity of gas phase and water phase, respectively.

Based on multiphase version of Darcy's law for fluid flow in porous media, the superficial velocity of phase  $j$  ( $j = g$  for gas phase and  $j = w$  for water phase) becomes

$$\vec{u}_j = -\frac{\vec{k} k_{rj}}{\mu_j} (\nabla p_j - \gamma_j \nabla D) \quad (6)$$

$k_{rj}$  is relative permeability,  $\mu_j$  is viscosity,  $\gamma_j$  is the specific weight of phase  $j$ , and  $D$  is depth.

The source term is written as

$$R_i = \frac{q_i}{V_b} \quad (7)$$

where  $q_i$  is the molar flow rate of component  $i$  which is positive for injection and negative for production,  $V_b$  is the bulk volume of a gridblock.

The final mass conservation equations for gas and water components are described below:

$$\frac{\partial}{\partial t} [\phi S_g (1 - c_{ag}) \xi_g + (1 - \phi) \rho_s v_{ag} \xi_{ag}] + \vec{\nabla} \cdot (\xi_g \vec{u}_g) - \frac{q_g}{V_b} = 0 \quad (8)$$

$$\frac{\partial}{\partial t} (\phi S_w \xi_w) + \vec{\nabla} \cdot (\xi_w \vec{u}_w) - \frac{q_w}{V_b} = 0 \quad (9)$$

**Gas desorption effect.** In our previous studies,<sup>9</sup> it was found that four experimental measurements of methane adsorption from the Marcellus Shale core samples deviate from the Langmuir isotherm, but obey the BET isotherm.<sup>57</sup> The standard BET isotherm assumes that the number of adsorption layers is infinite. Here, a general form of BET isotherm considering  $n$  adsorption layers is used as follows:

$$v_{ag} = \frac{v_m C p/p_o}{1 - p/p_o} \left[ \frac{1 - (n+1)(p/p_o)^n + n(p/p_o)^{n+1}}{1 + (C-1)p/p_o - C(p/p_o)^{n+1}} \right] \quad (10)$$

where  $v_{ag}$  is the gas volume of adsorption,  $p_o$  is the saturation pressure of the gas,  $v_m$  is the maximum adsorption gas volume when the adsorbent surface is being covered with a complete monomolecular layer,  $C$  is a constant. It is important to note that the saturation pressure loses its physical meaning when the reservoir temperature is above the critical methane temperature.<sup>58</sup>

Instead, the saturation pressure can be treated as pseudo-saturation pressure ( $p_s$ ) for the high-pressure/temperature methane adsorption,<sup>59</sup> which can be calculated using the following extrapolation of the Antoine equation:<sup>60-61</sup>

$$\ln p_s = 7.7437 - \frac{1306.5485}{19.4362 + T} \quad (11)$$

where  $T$  is temperature in K and  $p_s$  is pseudo-saturation pressure in MPa. After calculation of  $p_s$ , three parameters such as  $v_m$ ,  $n$ , and  $C$  are generally used to fit the experimental data of methane adsorption. When  $n=1$ , the general BET isotherm will be simplified as the classic Langmuir isotherm:<sup>62</sup>

$$v_{ag} = \frac{v_L p}{p + p_L} \quad (12)$$

where  $v_L$  is Langmuir volume (scf/ton), which is the maximum adsorbed gas volume at the infinite pressure,  $p_L$  is Langmuir pressure, which is the pressure at which one-half of the gas is desorbed.

**Adsorbed gas porosity.** In this study, the adsorbed gas density of methane is calculated by the expression proposed by Riewchotisakul and Akkutlu,<sup>63</sup> which is obtained based on the non-equilibrium molecular dynamic simulation to account for the change of adsorbed phase density with pressure in organic nanopores:

$$\rho_{ag} = 0.1057 \ln(p) - 0.4629 \quad (13)$$

where  $\rho_{ag}$  is the adsorbed gas density in g/cm<sup>3</sup> and  $p$  is pressure in psi. The variations of nanopore properties<sup>64</sup> such as pore size, shape and roughness are not considered in this expression. Note that the molar density of adsorbed gas can be calculated by



$$\xi_{ag} = \frac{\rho_{ag}}{M_{ag}} \quad (14)$$

where  $M_{ag}$  is molecular weight of adsorbed gas. Hence, the pore volume occupied by adsorbed gas can be calculated by

$$c_{ag} = \frac{(1-\phi)\rho_s v_{ag}\rho_{g,ST}}{\rho_{ag}\phi} \quad (15)$$

where  $\rho_{g,ST}$  is gas density at standard condition. Hence, the adsorbed gas porosity ( $\phi_{ag}$ ) is obtained as

$$\phi_{ag} = \frac{(1-\phi)\rho_s v_{ag}\rho_{g,ST}}{\rho_{ag}} \quad (16)$$

It should be pointed out that the adsorbed gas porosity should satisfy the criterion of  $0 \leq \phi_{ag} < \phi$ .

Since the formation is assumed to be slightly compressible, the porosity is a function of pressure and calculated by

$$\phi = \phi_o [1 + c_f(p - p_o)] \quad (17)$$

where  $\phi_o$  is the porosity at the reference pressure  $p_o$ ,  $c_f$  is the formation compressibility.

Accordingly, the porosity change for free gas not only considers the assumption of slightly compressible formation but also the pore volume occupied by adsorbed gas.

**Gas slippage and diffusion effect.** In shale formations, a large amount of nanopores result in the presence of multiple gas flow regimes. Gas slippage and diffusion effect becomes important in shale nanopores, especially at low pressure with reservoir depletion. Four flow regimes were proposed by Karniadakis and Beskok<sup>65</sup> depending on the Knudsen number ( $K_n$ ): (1) continuum flow regime ( $K_n < 0.01$ ); (2) slip-flow regime ( $0.01 < K_n < 0.1$ ); (3) transition regime (

$0.1 < K_n < 10$ ); and (4) free molecular flow regime ( $K_n > 10$ ). The Knudsen number is defined by

$$K_n = \frac{\lambda}{d} \quad (18)$$

where  $d$  is the pore diameter and  $\lambda$  is the mean free path of gas molecules, which is computed by<sup>66</sup>

$$\lambda = \frac{k_B T}{\sqrt{2} \pi \sigma^2 p} \quad (19)$$

where  $k_B$  is the Boltzmann constant ( $1.3805 \times 10^{-23}$  J/K),  $T$  is temperature in K,  $p$  is pressure in Pa, and  $\sigma$  is diameter of gas molecules.

For shale gas reservoirs with low and ultra-low permeability, the following apparent permeability model proposed by Florence et al.<sup>67</sup> is used to account for the gas slippage and diffusion effect:

$$k_a = k_i \left[ 1 + \alpha(K_n) K_n \right] \left( 1 + \frac{4K_n}{1 + K_n} \right) \quad (20)$$

where  $k_a$  is apparent matrix permeability,  $k_i$  is the initial matrix permeability,  $\alpha(K_n)$  represents the rarefaction parameter, which can be calculated by<sup>65</sup>

$$\alpha(K_n) = \frac{128}{15\pi^2} \tan^{-1}(4K_n^{0.4}) \quad (21)$$

Similarly, the other existing apparent permeability models considering complex nanopore phenomena such as surface diffusion of adsorbed gas in the literature can be easily added in the current numerical model.<sup>3,5-7,68</sup> However, the comparison of different apparent permeability models is beyond the scope of this study.

**Non-Darcy flow effect.** It is assumed that the non-Darcy flow effect only occurs for gas flow inside fractures. The non-Darcy flow is widely modeled using the Forchheimer modification to Darcy's law and is written as

$$-\nabla\Phi_g = \frac{\mu_g}{k \cdot k_{rg}} \vec{u}_g + \beta_g \rho_g |\vec{u}_g| \vec{u}_g \quad (22)$$

where  $\Phi_g$  is the potential of gas phase,  $\rho_g$  is gas density,  $\beta_g$  is the non-Darcy Forchheimer coefficient, which can be determined using the correlation proposed by Evans and Civan<sup>69</sup> as given below:

$$\beta_g = \frac{1.485 \times 10^9}{k^{1.021}} \quad (23)$$

where the unit of permeability is md and the unit of  $\beta_g$  is  $\text{ft}^{-1}$ . This correlation was obtained based on more than 180 data points including those for propped fractures and a good match is obtained with a correlation coefficient of 0.974.<sup>28</sup> This correlation will be implemented into the numerical model in this study.

**Pressure-dependent matrix permeability.** We use the empirical equation developed by Jones<sup>70</sup> according to experimental data to handle the correlation between the change of matrix permeability and net effective stress as follows:

$$\frac{k}{k_i} = \exp\left\{a_k \left[\exp(-\sigma_e/\sigma^*) - 1\right]\right\} / (1 + C' \sigma_e) \quad (24)$$

where  $a_k$  is a constant,  $\sigma^*$  is a decay constant, which is arbitrarily given as 3,000 psi,  $C'$  is a constant, which is arbitrarily set to  $3 \times 10^{-6} \text{ psi}^{-1}$ ,<sup>70</sup>  $\sigma_e$  is the net effective stress, which is defined by

$$\sigma_e = \sigma - \alpha p_r \quad (25)$$

where  $\sigma$  is the confining stress,  $p_r$  is pore pressure,  $\alpha$  is Biot's constant, which can be calculated for an ideal uniaxial strain scenario:<sup>71</sup>

$$\alpha = 1 - \frac{c_m}{c_b} \quad (26)$$

where  $c_m$  is rock matrix compressibility and  $c_b$  is rock bulk compressibility.

**Pressure-dependent fracture permeability.** It has been recognized that fracture conductivity, which refers to fracture permeability multiplied by fracture width, is challenging to maintain a constant high value in reality, whereas it often declines with the increasing closure pressure due to proppant embedment, proppant crushing etc. This phenomenon is more serious when the shale rock is soft. Through fitting the laboratory measurement data for different shale core samples ranging from stiff to soft (Figure 1),<sup>20</sup> the relationships between normalized fracture conductivity and closure pressure were obtained below:<sup>72</sup>

$$\text{Stiff shale: } \log(FC_N) = -0.0001 \times \sigma_c - 0.1082, R^2 = 0.954 \quad (27)$$

$$\text{Medium shale: } \log(FC_N) = -0.0004 \times \sigma_c + 0.2191, R^2 = 0.998 \quad (28)$$

$$\text{Soft shale: } \log(FC_N) = -0.0006 \times \sigma_c - 0.4256, R^2 = 0.987 \quad (29)$$

where  $FC_N$  is normalized fracture conductivity divided by the initial fracture conductivity, and  $\sigma_c$  is closure pressure in psi. The above equations will be implemented in the numerical model in this study.

## Embedded Discrete Fracture Model

We use the state-of-the-art EDFM approach to handle complex fracture geometries. The EDFM has been approved to be a powerful method to model complex fracture geometries in unconventional oil and gas reservoir simulation. The EDFM method borrows concepts from both

dual-continuum model and discrete fracture models. In this method, a fracture with any shape is discretized into small segments based on the matrix block boundaries. Correspondingly, in the computational domain, some additional virtual cells are created to represent these segments. To accurately simulate fluid flow associated with these fracture segments, the non-neighboring connections (NNCs) are defined for these virtual blocks and transmissibility factors are calculated.

In the EDFM approach, all connections can be classified into four basic types, including flow between matrix blocks and fractures, flow between fracture segments inside an individual fracture, flow between intersecting fracture segments, and flow between fracture segment and the wellbore it intersects. The first three types of connections are simulated using transmissibility factors between blocks, and the volume flow rate ( $q$ ) of phase  $l$  between blocks in a NNC pair can be express as

$$q = \lambda_l T_{NNC} \Delta p \quad (30)$$

where  $\lambda_l$  is the relative mobility of phase  $l$ ,  $T_{NNC}$  is the transmissibility factor, and  $\Delta p$  is the potential difference between corresponding blocks.

Generally,  $T_{NNC}$  can be expressed as

$$T_{NNC} = \frac{k_{NNC} A_{NNC}}{d_{NNC}} \quad (31)$$

where  $k_{NNC}$ ,  $A_{NNC}$ , and  $d_{NNC}$  represent the permeability, common area, and distance for the connection, respectively.

For flow between fracture and matrix,  $k_{NNC}$  is the matrix permeability,  $A_{NNC}$  is the area of the fracture segment, and  $d_{NNC}$  is the average normal distance from matrix block to fracture segment.

For flow between fracture segments (within individual fracture or between intersecting fractures),  $k_{NNC}$  is the fracture permeability,  $A_{NNC}$  is the common area between fracture segments, and  $d_{NNC}$  is the distance between fracture segments.

Similarly, fracture-wellbore intersections are modeled by treating fracture segments as wellblocks and assigning well indices. The calculation of well indices is similar to Peaceman's model. More details of the transmissibility factor and well index calculation can be found in Moinfar et al.<sup>40</sup> and Xu et al.<sup>32</sup>

Finally, the finite difference method is utilized to solve the coupled and highly nonlinear partial differential equations. Under the assumption of isothermal shale-gas reservoir, the unknowns should be specified initially include reservoir pressure and the number of moles for each component. In addition, no flow boundary condition is considered. An implicit pressure, explicit composition technique is used to solve for the unknowns such as pressure and component moles. More details can be found in the work by Chang.<sup>73</sup> The physical properties of real gas such as density, viscosity and compressibility are calculated using Peng-Robinson equation of state.<sup>74-75</sup>

### Model Verification for Planar Hydraulic Fractures

We set up a basic 3D reservoir model with dimensions of 2020 ft × 1500 ft × 130 ft (615.70 m × 457.20 m × 39.624 m), which corresponds to reservoir length, width, and thickness, respectively, as shown in Figure 2. The dimension of grid size is 20 ft × 20 ft × 130 ft (6.096 m × 6.096 m × 39.624 m). A synthetic shale-gas case with 11 planar hydraulic fractures was simulated with the

purpose of verifying the new developed model against a commercial reservoir simulator.<sup>76</sup> The commercial simulator utilizes the LGR approach to handle hydraulic fracture. Each block containing hydraulic fracture is refined by  $5 \times 1 \times 1$ . Our model uses the EDFM approach to deal with hydraulic fracture without the need of grid refinement near the fracture. The other reservoir and fracture properties used for the simulations are summarized in Table 1. The gas type is methane. The reservoir is assumed to be homogeneous with two phase flow of gas and water. The initial water saturation is assumed to be 50% for the purpose of verification. It should be mentioned that the effects of capillary pressure and nanopore confinement on fluid transport are not included in the current study,<sup>77</sup> which will be examined in detail in our future study. Figure 3 presents different relative permeability curves for the matrix and fracture system, respectively.

The constant flowing bottomhole pressure (BHP) of 500 psi (3.45 MPa) is assumed for the simulation constraint over time. Fracture height is assumed to fully penetrate reservoir thickness. Gas desorption is considered using Langmuir isotherm, which is available in the commercial reservoir simulator. Note that the influence of the existing water phase on gas adsorption capacity is not considered in this study, which needs more fundamental research. The non-Darcy flow effect for both hydraulic and natural fractures is considered using the non-Darcy Forchheimer coefficient proposed by Evans and Civan.<sup>69</sup>

Figure 4 compares the simulation results of both flow rates and cumulative production for gas and water at a 30-year period between our model and the commercial reservoir simulator. As can be seen, a good match is obtained between them. It implies that our numerical model in conjunction with the EDFM approach can simulate shale-gas production with planar fractures by considering gas desorption and non-Darcy flow effects. Figure 5 shows the pressure distribution

after 30 years of production. It can be observed that the effective drainage area can be clearly demonstrated.

## Complex Gas Transport Mechanisms

In the following sections, we examined the impacts of complex gas transport mechanisms on well performance such as gas desorption, gas slippage and diffusion in more detail. It is important to point out that the initial water saturation is changed to 20%, which is the residual water saturation. Hence, there is only gas flow for the following case studies. The other input parameters remain the same as those in Table 1.

**Gas desorption effect.** In our previous study associated with gas desorption,<sup>9</sup> it has been found that the BET isotherm performs a better match than Langmuir isotherm with the measured methane adsorption under high reservoir pressure, as shown in Figure 6. The fitting parameters of BET isotherm such as  $v_m = 49.01$  scf/ton,  $C = 24.56$ , and  $n = 4.46$  are used in this study. Figure 7 shows the effects of gas adsorption using BET isotherm with and without considering adsorbed gas porosity on well performance. It can be illustrated that the relative contribution of gas desorption on well performance after 30 years without considering the adsorbed gas porosity is around 11% compared to the case without considering gas desorption. However, it will decrease to around 5% when considering the adsorbed gas porosity. Hence, the adsorbed gas porosity effect significantly affects well performance, which has been usually neglected in the literature.

**Gas slippage and diffusion effect.** Figure 8 presents the effect of gas slippage and diffusion on well performance by considering various nanopore sizes between 5 nm to 50 nm. It can be observed that the smaller the nanopore size, the higher ultimate gas recovery. This is because the smaller pore size leads to larger Knudsen number, and then the ratio of apparent permeability to



initial matrix permeability in Eq. 20 increases accordingly, especially at lower reservoir pressure, resulting in higher gas recovery. The positive contribution of gas slippage and diffusion effect to ultimate gas recovery after 30 years is about 13% and 7% with respect to the nanopore size 5 nm and 10 nm, respectively, when compared to the case without considering the effect. However, the nanopore size of 50 nm has negligible impact on well performance in this study.

Figure 9 shows the combining effects of gas desorption, adsorbed gas porosity, gas slippage and diffusion discussed in the preceding on well performance. The nanopore size of 5 nm is assumed. It clearly shows that a significant increase of ultimate gas recovery of 18% after 30 years of production is determined when compared to the case without considering the combining effects.

Figure 10 shows the comparison of pressure distribution after 30 years with and without considering the combining effects. As shown, a faster reservoir depletion occurs when considering the combining effects. Accordingly, it can be concluded that it is extremely important to consider all of these important complex gas transport mechanisms in nanopores and organic matter in order to accurately simulate shale gas production.

### **Natural Fracture Effect**

Next, the effect of natural fractures in combination with 11 planar hydraulic fractures described in the preceding on well performance is investigated. We designed three cases with different number and set of natural fractures, as shown in Figure 11. Case 1 is with 100 one-set natural fractures. Case 2 is with 200 one-set natural fractures. Case 3 is with 200 two-set natural fractures. It should be pointed out that a statistical method was used to generate the natural fracture properties, which are normally distributed in the reservoir of interest. For cases 1 and 2, the natural fractures are oriented at 5-10 degree along the horizontal wellbore, which are almost

perpendicular to hydraulic fractures. The natural fractures length ranges from 100 ft (30.48 m) to 300 ft (91.44 m). For Case 3, one set of natural fractures is oriented at 45-55 degree and another set is 135-145 degree. Similarly, the length of natural fractures ranges from 100 ft (30.48 m) to 300 ft (91.44 m). The conductivity of natural fractures for each case is assumed to be 10 md-ft ( $3.01 \times 10^{-15} \text{ m}^2\text{-m}$ ) and the conductivity of hydraulic fractures is 100 md-ft ( $3.01 \times 10^{-14} \text{ m}^2\text{-m}$ ). The natural fracture height is assumed equal to the reservoir thickness. The effects of non-Darcy flow, gas desorption, adsorbed gas porosity, and nanopore size of 5 nm are considered.

Figure 12 compares the effects of different number and sets of natural fractures on well performance. As shown, the natural fractures have a critical effect on well performance. The increase of ultimate gas recovery after 30 years compared to base case without natural fractures is 6.3%, 7.8%, and 23.2% for Cases 1, 2, and 3, respectively. Figure 13 shows the comparison of pressure distribution after 1000 days and 30 years of production for each case. It can be clearly demonstrated that there is a larger effective drainage area for cases 1-3 than that for base case without natural fractures [Figures 13a and 13b]. In addition, there is a little difference between Case 1 and Case 2. This is because the number of natural fractures connected with hydraulic fractures increase slightly with an increase of fracture number from 100 to 200, resulting in a little bit increase of drainage area [Figures 13e and 13f vs. Figures 13c and 13d]. However, there are more number of natural fractures connected to hydraulic fractures directly or indirectly for Case 3, leading to a much more complex connected fracture network and a bigger expansion of drainage area than cases 1 and 2 [Figures 13g and 13h]. Hence, it can be predicted that it is important to create a better connected complex fracture network during the actual fracturing process, which is vital to maximizing the stimulation effectiveness and production optimization.

The influences of detailed natural fracture conductivity, density, orientation, distribution on well performance will be examined in more detail in our future study.

### **Complex Non-Planar Fracture Geometry**

In this study, a complex hydraulic fracture propagation model, developed by Wu and Olson,<sup>78</sup> is used to predict complex non-planar fracture geometry through modeling the interaction between hydraulic fractures and natural fractures. The model couples rock deformation and fluid flow in the fractures and horizontal wellbore. The core solid mechanics solution is three dimensional, such that fracture opening, shearing and stress shadow effects are accurately determined for single and multi-fracture cases.<sup>15</sup> Fluid flow in the fracture and the associated pressure drop are based on lubrication theory, assuming the fracture is analogous to a slot between parallel plates and the fluid is non-Newtonian. A constant total fluid injection rate is given. Partitioning of flow rate into each fracture is dynamically calculated in such way that the wellbore pressure is constrained to gradually decrease along the lateral due to wellbore friction. The interaction of hydraulic and natural fractures is described through analyzing induced stresses at the fracture tips. Stochastic realization methods were used to describe natural fracture patterns.<sup>78</sup> Length of natural fractures follows a power-law distribution. The model has been validated against known analytical solutions for single hydraulic fracture growth.<sup>79</sup> To demonstrate the validity of capturing the physical process of fracture interaction, the model has also been compared to a numerical model<sup>12</sup> in case of multiple fracture propagation. The primary assumptions for the current fracture model include: transverse fractures are initiated perpendicular to the horizontal wellbore with a nominal initial length; fracture height is constant; proppant transport and poroelastic effects are not considered. In this study, the parameters used for the fracture model include fluid injection rate of 20 barrels per minute (bbl/min) and injection time of 10 minutes

for each fracture, Young's modulus of  $3 \times 10^6$  psi ( $2.07 \times 10^4$  MPa), Poisson ratio of 0.23, the difference of minimum and maximum horizontal stress of 500 psi, and fluid leak-off coefficient of  $5 \times 10^{-3}$  ft/min<sup>0.5</sup> ( $1.524 \times 10^{-3}$  m/min<sup>0.5</sup>). Figure 14 shows the distribution of fracture width of the generated complex non-planar fracture geometry for a synthetic shale-gas case. For this case study, there are 11 non-planar fractures evenly spaced 140 ft (42.672 m) and 100 natural fractures. As shown, the distribution of fracture width is highly non-uniform.

Next, the complex fracture geometry was transformed to reservoir model, as shown in Figure 15. The non-uniform fracture width results in varying fracture conductivity across the fractures ranging from 0.1 md-ft ( $3.01 \times 10^{-17}$  m<sup>2</sup>-m) to 48 md-ft ( $14.45 \times 10^{-15}$  m<sup>2</sup>-m). The natural fracture conductivity is 10 md-ft ( $3.01 \times 10^{-15}$  m<sup>2</sup>-m). The other input parameters are kept the same as those in Table 1. The combining effects of non-Darcy flow, gas desorption, adsorbed gas porosity, and nanopore size of 5 nm are considered. In addition, the effects of pressure-dependent matrix permeability and fracture conductivity are included. We use Eq. 24 with  $a_k$  of 2.7442 and Eq. 28 to generate the pressure-dependent matrix permeability and fracture conductivity, respectively, as shown in Figure 16. Here, it should be mentioned that both hydraulic and natural fractures are assumed to use the same generated pressure-dependent fracture conductivity curve in this study. Different curves for different fractures will be investigated in our future study. The normalized decline rate means that the matrix permeability and fracture conductivity at different pressure divided initial matrix permeability and fracture conductivity. As shown, the matrix permeability and fracture conductivity at BHP of 500 psi (3.45 MPa) are about 20% and 8% of initial values for this case study. Figure 17 presents the effects of pressure-dependent matrix permeability and fracture conductivity on well performance individually or simultaneously. It can be clearly

observed that pressure-dependent effect significantly declines the gas recovery. The ultimate gas recovery after 30 years is decreased by 16%, 20%, and 31% for pressure-dependent matrix permeability, fracture conductivity, and both, respectively, when compared to the case without considering these effects. Figure 18 presents the comparison of pressure distribution of different scenarios after 1000 days and 30 years. As shown, the drainage area is mainly concentrated nearby the fractures when only considering pressure-dependent matrix permeability [Figures 18c and 18d vs. Figures 18a and 18b]. However, when only taking into account pressure-dependent fracture conductivity, the effective drainage area becomes further smaller after 1000 days [Figure 18c vs. Figure 18e], whereas the reservoir depletion becomes more wider after 30 years due to the dominate role of matrix permeability at later times [Figure 18d vs. Figure 18f]. When the effects of pressure-dependent of both matrix permeability and fracture conductivity are included, the drainage area and reservoir depletion are much smaller than the case without these effects [Figures 18g and 18h vs. Figures 18a and 18b]. Hence, it is highly recommended that pressure-dependent rock and fracture properties should be carefully characterized based on laboratory measurements in order to achieve an optimal treatment design in shale gas reservoirs.

Finally, we investigate the impact of reservoir heterogeneity on well performance. A range of matrix permeability between 0.0001 md (100 nD) and 0.001 md (1000 nD) is considered. Figure 19 represents the distribution of matrix permeability in the reservoir. Correspondingly, the average equivalent matrix permeability is calculated as about 0.0005 md (500 nD). The comparison of well performance between the homogeneous and heterogeneous scenarios is shown in Figure 20. It can be clearly seen that the relative difference of ultimate gas recovery after 30 years between the heterogeneous case and the homogeneous case with the minimum

permeability of 0.0001 md is as high as 35%. It is about 27% between the heterogeneous case and the homogeneous case with the maximum permeability of 0.001 md. However, the difference between the heterogeneous case and the homogeneous case with average equivalent permeability of 0.0005 md is small, which is about 5% after 30 years. Hence, it is important to properly characterize the distribution of matrix permeability in order to perform a better production prediction in shale gas reservoirs.

## Conclusions

In this study, we developed a new multi-mechanism numerical model through fully incorporating a state-of-the-art EDFM approach to simulate shale gas production more accurately and efficiently. A good match of two-phase (gas/water) flow between the new model and the commercial reservoir simulator was obtained for a shale-gas case with planar hydraulic fractures. The impacts of various gas transport physics, natural fractures, non-planar fractures, pressure-dependent rock and fracture properties and heterogeneity on well performance were investigated in more detail. The following conclusions can be drawn based on the simulation results of this study:

- (1) The gas desorption effect without considering the adsorbed gas density may overestimate the ultimate gas production. An overestimate of ultimate gas production of 6% after 30 years was observed in this study.
- (2) Gas slippage and diffusion effect in shale nanopores significantly impacts well productivity.

The ultimate gas production after 30 years can be increased by about 13% with nanopore size of 5 nm. However, this effect might become less important when nanopore size is in excess of a critical value, for example, 50 nm in this study.

- (3) The combining effects of non-Darcy flow, gas desorption, adsorbed gas porosity, gas slippage and diffusion are important physics for affecting well performance. A significant increase of gas recovery of 18% after 30 years was achieved compared with the case ignoring these components.
- (4) The number of set of natural fractures has a great effect on well performance due to the formation of a more connected complex fracture networks. Two-set natural fractures contributes to an increase of gas recovery of 23.2% after 30 years, whereas one-set natural fracture only contributes to an increase of gas recovery of 7.8% under the same number of 200.
- (5) This model allows to handle complex non-planar fracture geometry with varying fracture width and fracture conductivity along fracture length, which is generated by a complex hydraulic fracture propagation model.
- (6) Pressure-dependent matrix permeability and fracture conductivity effects have a significant negative influence on well performance and reservoir drainage efficiency. A significant reduction of gas recovery of 31% after 30 years was obtained compared with the case without considering these effects. Detailed laboratory measures of pressure-dependent shale and fracture properties are highly recommended in order to accurately evaluate well performance and stimulation effectiveness.
- (7) Heterogeneity of matrix permeability plays a vital role in well productivity. A big difference of 35% and 27% was observed between the heterogeneous case and the homogeneous case with the minimum permeability of 0.0001 md and the maximum permeability of 0.001 md, respectively. The converted equivalent average matrix permeability has a small difference of well performance compared with the heterogeneous case.

## Acknowledgments

The authors would like to acknowledge financial supports from Texas A&M Engineering Experiment Station (TEES) and National Natural Science Foundation of China (Grant No. 51728401). We would also like to acknowledge Computer Modeling Group Ltd. for providing the CMG-GEM software for this study.

## Notation

EDFM = Embedded Discrete Fracture Model

BET = Brunauer, Emmett and Teller

EIA = Energy Information Administration

LGR = Local grid refinement

NNCs = Non-neighboring connections

BHP = Bottomhole pressure

MMscf =  $10^6$  Standard cubic feet

scf = standard cubic feet

$W_i$  = the accumulation term, lb-moles/ft<sup>3</sup>/s

$\vec{F}_i$  = the flux term, lb-moles/ft<sup>3</sup>/s

$R_i$  = the source term, lb-moles/ft<sup>3</sup>/s

$t$  = time, second

$\phi$  = porosity

$S_g$  = gas saturation

$c_{ag}$  = volume fraction of adsorbed gas per unit pore volume

$\xi_g$  = molar density of gas phase, lb-mole/ft<sup>3</sup>



$\rho_s$	=	rock density, ton/ft <sup>3</sup>
$v_{ag}$	=	specific volume of gas adsorbed per unit mass of bulk rock, scf/ton
$\xi_{ag}$	=	molar density of adsorbed gas, lb-mole/ft <sup>3</sup>
$\xi_w$	=	molar density of water phase, lb-mole/ft <sup>3</sup>
$S_w$	=	water saturation
$\bar{u}_g$	=	superficial velocity of gas phase, m/s
$\bar{u}_w$	=	superficial velocity of water phase, m/s
$k_{rj}$	=	relative permeability of phase $j$
$\mu_j$	=	viscosity of phase $j$ , cp
$\gamma_j$	=	specific weight of phase $j$
$D$	=	depth, ft
$q_i$	=	molar flow rate of component $i$ , lb-mole/s
$V_b$	=	bulk volume of a gridblock, ft <sup>3</sup>
$v_{ag}$	=	gas volume of adsorption, scf/ton
$p_o$	=	saturation pressure of the gas, psi
$v_m$	=	the maximum adsorption gas volume, scf/ton
$C$	=	a constant value
$T$	=	temperature, K
$p_s$	=	pseudo-saturation pressure, MPa
$v_L$	=	Langmuir volume, scf/ton
$p_L$	=	Langmuir pressure, psi
$\rho_{ag}$	=	adsorbed gas density, g/cm <sup>3</sup>

$p$	=	pressure, psi
$M_{ag}$	=	molecular weight of adsorbed gas, kg/mole
$\rho_{g,ST}$	=	gas density at standard condition, g/cm <sup>3</sup>
$\phi_o$	=	porosity at the reference pressure $p_o$
$c_f$	=	formation compressibility, 1/psi
$K_n$	=	Knudsen number
$d$	=	the pore diameter, nm
$\lambda$	=	the mean free path of gas molecules, nm
$k_B$	=	the Boltzmann constant, J/K
$\sigma$	=	diameter of gas molecules
$k_a$	=	apparent matrix permeability, md
$k_i$	=	initial matrix permeability, md
$\alpha(K_n)$	=	the rarefaction parameter
$\Phi_g$	=	potential of gas phase, psi
$\rho_g$	=	gas density, g/cm <sup>3</sup>
$\beta_g$	=	the non-Darcy Forchheimer coefficient, 1/ft
$a_k$	=	a constant value
$\sigma^*$	=	a decay constant, psi
$C'$	=	a constant value, 1/psi
$\sigma_e$	=	net effective stress, psi
$\sigma$	=	the confining stress, psi
$p_r$	=	pore pressure, psi

$\alpha$	=	Biot's constant
$c_m$	=	rock matrix compressibility, 1/psi
$c_b$	=	rock bulk compressibility, 1/psi
$FC_N$	=	normalized fracture conductivity
$\sigma_c$	=	closure pressure, psi
$\lambda_l$	=	relative mobility of phase $l$ , $\text{cp}^{-1}$
$T_{NNC}$	=	transmissibility factor, md-ft
$\Delta p$	=	potential difference between corresponding blocks, psi
$q$	=	volume of flow rate, $\text{ft}^3/\text{d}$
$k_{NNC}$	=	permeability for the connection, md
$A_{NNC}$	=	common area for the connection, $\text{ft}^2$
$d_{NNC}$	=	distance for the connection, ft

SI Metric Conversion Factors

ft	×	3.048	e-01	=	m
ft <sup>3</sup>	×	2.832	e-02	=	m <sup>3</sup>
cp	×	1.0	e-03	=	Pa·s
psi	×	6.895	e+00	=	kPa
md	×	1e-15	e+00	=	m <sup>2</sup>
days	×	8.64	e+4	=	seconds
ton	×	9.072	e+02	=	kg
°F	(°F-32)/1.8	=	°C		

Literature Cited

1. Cipolla CL, Lolon EP, Erdle JC, Rubin B. Reservoir modeling in shale-gas reservoirs. *SPE Reservoir Eval Eng.* 2010;13(4):638-653.
2. Energy Information Administration. Shale gas production drives world natural gas production growth. 2016. <http://www.eia.gov/todayinenergy/detail.cfm?id=27512>.
3. Javadpour F, Fisher D, Unsworth M. Nanoscale gas flow in shale gas sediments. *J Can Petrol Technol.* 2007;46(10):55-61.
4. Wang FP, Reed RM. Pore networks and fluid flow in gas shales. SPE Annual Technical Conference and Exhibition, New Orleans, Louisiana, 2009.
5. Civan F. Effective correlation of apparent gas permeability in tight porous media. *Transport Porous Med.* 2010;82(2):375-384.
6. Civan F, Rai CS, Sondergeld CH. Shale-gas permeability and diffusivity inferred by improved formulation of relevant retention and transport mechanisms. *Transport Porous Med.* 2011;86(3):925-944.
7. Sakhaee-Pour A, Bryant SL. Gas permeability of shale. *SPE Reservoir Eval Eng.* 2012;15(4):401-409.
8. Akkutlu IY, Fathi E. Multi-scale gas transport in shales with local kerogen heterogeneities. *SPE J.* 2012;17(4):1002-1011.
9. Yu W, Sepehrnoori K, Patzek TW. Modeling gas adsorption in Marcellus shale with Langmuir and BET isotherms. *SPE J.* 2016a;21(2):589-600.
10. Warpinski NR, Kramm RC, Heinze JR, Waltman CK. Comparison of single and dual-array microseismic mapping techniques in the Barnett shale. SPE Annual Technical Conference and Exhibition, Dallas, Texas, 2005.

11. Cipolla CL, Wallace J. Stimulated reservoir volume: a misapplied concept? SPE Hydraulic Fracturing Technology Conference, The Woodlands, Texas, 2014.
12. Wu R, Kresse O, Weng X, Cohen C, Gu H. Modeling of interaction of hydraulic fractures in complex fracture networks. SPE Hydraulic Fracturing Technology Conference, The Woodlands, Texas, 2012.
13. Xu G, Wong SW. Interaction of multiple non-planar hydraulic fractures in horizontal wells. International Petroleum Technology Conference, Beijing, China, 2013.
14. Wu K, Olson JE. Investigation of the impact of fracture spacing and fluid properties for interfering simultaneously or sequentially generated hydraulic fractures. *SPE Prod Oper.* 2013;28(4):427-436.
15. Wu K, Olson JE. Simultaneous multifracture treatments: fully coupled fluid flow and fracture mechanics for horizontal wells. *SPE J.* 2015;20(2):337-346.
16. Weijers L, de Pater CJ. Fracture reorientation in model tests. SPE Formation Damage Control Symposium, Lafayette, Louisiana, 1992.
17. Abass HH, Hedayati S, Meadows DL. Nonplanar fracture propagation from a horizontal wellbore: experimental study. *SPE Prod Facil.* 1996;11(3):133-137.
18. LaFollette RF, Carman PS. Proppant diagenesis: results so far. SPE Unconventional Gas Conference, Pittsburgh, Pennsylvania, 2010.
19. Fan L, Thompson JW, Robinson JR. Understanding gas production mechanism and effectiveness of well stimulation in the Haynesville shale through reservoir simulation. Canadian Unconventional Resources and International Petroleum Conference, Calgary, Canada, 2010.

20. Alramahi B, Sundberg MI. Proppant embedment and conductivity of hydraulic fractures in shales. 46<sup>th</sup> US Rock Mechanics/Geomechanics Symposium, Chicago, Illinois, 2012.
21. Chen CC, Raghavan R. A multiply-fractured horizontal well in a rectangular drainage region. *SPE J.* 1997;2(4):455-465.
22. Zhou W, Banerjee R, Poe BD, Spath J, Thambynayagam M. Semi-analytical production simulation of complex hydraulic-fracture networks. *SPE J.* 2014;19(1):6-18.
23. Yu W, Wu K, Sepehrnoori K. A semianalytical model for production simulation from nonplanar hydraulic-fracture geometry in tight oil reservoirs. *SPE J.* 2016b;21(3):1028-1040.
24. Yang R, Huang Z, Yu W, Li G, Ren W, Zuo L, Tan X, Sepehrnoori K, Tian S, Sheng M. A comprehensive model for real gas transport in shale formations with complex non-planar fracture networks. *Sci Rep.* 2016;6:36673.
25. Chen Z, Liao X, Zhao X, Lyu S, Zhu L. A comprehensive productivity equation for multiple fractured vertical wells with non-linear effects under steady-state flow. *J Pet Sci Eng.* 2017;149:9-24.
26. Yu W, Wu K, Sepehrnoori K, Xu W. A comprehensive model for simulation of gas transport in shale formation with complex hydraulic-fracture geometry. *SPE Reservoir Eval Eng.* 2017a;20(3):547-561.
27. Wang W, Yu W, Hu X, Liu H, Chen Y, Wu K, Wu B. A semianalytical model for simulating real gas transport in nanopores and complex fractures of shale gas reservoirs. *AIChE J.* 2017; in press.
28. Rubin B. Accurate simulation of non-Darcy flow in stimulated fractured shale reservoirs. SPE Western Regional Meeting, Anaheim, California, 2010.

29. Yu W, Sepehrnoori K. Simulation of gas desorption and geomechanics effects for unconventional gas reservoirs. *Fuel*. 2014a;116:455-464.
30. Warren JE, Root PJ. The behavior of naturally fractured reservoirs. *SPE J*. 1963;3(3):245-255.
31. Dershowitz B, LaPointe P, Eiben T, Wei L. Integration of discrete feature network methods with conventional simulator approaches. SPE Annual Technical Conference and Exhibition, New Orleans, Louisiana, 1998.
32. Xu Y, Cavalcante Filho JSA, Yu W, Sepehrnoori K. Discrete-fracture modeling of complex hydraulic-fracture geometries in reservoir simulators. *SPE Reservoir Eval Eng*. 2017a;20(2):403-422.
33. Sandve TH, Berre I, Nordbotten JM. An efficient multi-point flux approximation method for discrete fracture–matrix simulations. *J Comput Phys*. 2012;231(9):3784-3800.
34. Mirzaei M, Cipolla CL. A workflow for modeling and simulation of hydraulic fractures in unconventional gas reservoirs. SPE Middle East Unconventional Gas Conference and Exhibition, Abu Dhabi, UAE, 2012.
35. Hui MH, Mallison BT, Fyrozjaee MH, Narr W. The upscaling of discrete fracture models for faster, coarse-scale simulations of IOR and EOR processes for fractured reservoirs. SPE Annual Technical Conference and Exhibition, New Orleans, Louisiana, 2013.
36. Edwards DA, Cheng N, Dombrowsky TP, Bowen G, Nasvik H. Representing hydraulic fractures using a multilateral, multisegment well in simulation models. SPE Reservoir Simulation Symposium, The Woodlands, Texas, 2013.
37. Du S, Yoshida N, Liang B, Chen J. Application of multi-segment well approach: dynamic modeling of hydraulic fractures. *J Nat Gas Sci Eng*. 2016;34:886-897.

38. Li L, Lee SH. Efficient field-scale simulation of black oil in a naturally fractured reservoir through discrete fracture networks and homogenized media. *SPE Reservoir Eval Eng.* 2008;11(4):750-758.
39. Hajibeygi H, Karvounis D, Jenny P. A hierarchical fracture model for the iterative multiscale finite volume method. *J Comput Phys.* 2011;230(24):8729-8743.
40. Moinfar A, Varavei A, Sepehrnoori K, Johns RT. Development of an efficient embedded discrete fracture model for 3D compositional reservoir simulation in fractured reservoirs. *SPE J.* 2014;19(2):289-303.
41. Panfili P, Cominelli A. Simulation of miscible gas injection in a fractured carbonate reservoir using an embedded discrete fracture model. Abu Dhabi International Petroleum Exhibition and Conference, Abu Dhabi, UAE, 2014.
42. Cavalcante Filho JSA, Shakiba M, Moinfar A, Sepehrnoori K. Implementation of a preprocessor for embedded discrete fracture modeling in an IMPEC compositional reservoir simulator. SPE Reservoir Simulation Symposium, Houston, Texas, 2015.
43. Shakiba M, Sepehrnoori K. Using embedded discrete fracture model (edfm) and microseismic monitoring data to characterize the complex hydraulic fracture networks. SPE Annual Technical Conference and Exhibition, Houston, Texas, 2015.
44. Yu W, Xu Y, Weijermars R, Wu K, Sepehrnoori K. Impact of well interference on shale oil production performance: a numerical model for analyzing pressure response of fracture hits with complex geometries. SPE Hydraulic Fracturing Technology Conference and Exhibition, The Woodlands, Texas, 2017b.



45. Wang K, Liu H, Luo J, Wu K, Chen, Z. A comprehensive model coupling embedded discrete fractures, multiple interacting continua, and geomechanics in shale gas reservoirs with multiscale fractures. *Energy Fuels*. 2017;31(8):7758-7776.
46. Xu Y. *Implementation and application of the Embedded Discrete Fracture Model (EDFM) for reservoir simulation in fractured reservoirs*. Master Thesis, The University of Texas at Austin, 2015.
47. Zuloaga-Molero P, Yu W, Xu Y, Sepehrnoori K, Li B. Simulation study of CO<sub>2</sub>-EOR in tight oil reservoirs with complex fracture geometries. *Sci Rep*. 2016;6:33445.
48. Zhang Y, Yu W, Sepehrnoori K, Di Y. A comprehensive numerical model for simulating fluid transport in nanopores. *Sci Rep*. 2017a;7:40507.
49. Zhang Y, Di Y, Yu W, Sepehrnoori K. A comprehensive model for investigation of CO<sub>2</sub>-EOR with nanopore confinement in the Bakken tight oil reservoir. SPE Annual Technical Conference and Exhibition, San Antonio, Texas, 2017b.
50. Xu Y, Yu W, Sepehrnoori K. Modeling dynamic behaviors of complex fractures in conventional reservoir simulators. SPE/AAPG/SEG Unconventional Resources Technology Conference, 24-26 July, Austin, Texas, 2017b.
51. Wu YS, Li J, Ding D, Wang C, Di Y. A generalized framework model for the simulation of gas production in unconventional gas reservoirs. *SPE J*. 2014;19(5):845-857.
52. Sun H, Chawathe A, Hoteit H, Shi X, Li L. Understanding shale gas flow behavior using numerical simulation. *SPE J*. 2015;20(1):142-154.
53. Li X, Zhang D, Li S. A multi-continuum multiple flow mechanism simulator for unconventional oil and gas recovery. *J Nat Gas Sci Eng*. 2015;26:652-669.

54. Fung LSK, Du S. Parallel-simulator framework for multipermeability modeling with discrete fractures for unconventional and tight gas reservoirs. *SPE J.* 2016;21(4):1370-1385.
55. An C, Fang Y, Liu S, Alfi M, Yan B, Wang Y, Killough J. Impacts of matrix shrinkage and stress changes on permeability and gas production of organic-rich shale reservoirs. SPE Reservoir Characterization and Simulation Conference and Exhibition, Abu Dhabi, UAE, 2017.
56. Lake LW. *Enhanced oil recovery*. Englewood Cliffs, New Jersey: Prentice Hall, 1989.
57. Brunauer S, Emmett PH, Teller E. Adsorption of gases in multimolecular layers. *J Am Chem Soc.* 1938;60:309-319.
58. Ozdemir E. *Chemistry of the adsorption of carbon dioxide by argonne permium coals and a model to simulate CO<sub>2</sub> sequestration in coal seams*. PhD Dissertation, University of Pittsburgh, 2004.
59. Clarkson CR, Bustin RM, Levy JH. Application of the monolayer/multilayer and adsorption potential theories to coal methane adsorption isotherms at elevated temperature and pressure. *Carbon.* 1997;35(12):1689-1705.
60. NIST. Thermophysical properties of fluid systems. 2011. <http://webbook.nist.gov/chemistry/fluid/>.
61. Hao S, Chu W, Jiang Q, Yu X. Methane adsorption characteristics on coal surface above critical temperature through Dubinin-Astakhov model and Langmuir model. *Colloids and Surfaces A: Physicochemical Engineering Aspects* 2014;444:104-113.
62. Langmuir I. The adsorption of gases on plane surfaces of glass, mica and platinum. *J Am Chem Soc.* 1918;40:1403-1461.

63. Riewchotisakul S, Akkutlu IY. Adsorption enhanced transport of hydrocarbons in organic nanopores. SPE Annual Technical Conference and Exhibition, Houston, Texas, 2015.
64. Wu K, Chen Z, Li X, Dong X. Methane storage in nanoporous material at supercritical temperature over a wide range of pressures. *Sci Rep.* 2016;6:33461.
65. Karniadakis GE, Beskok A. *Micro-flows, fundamentals and simulation*. New York: Spriger-Verlag, 2002.
66. Heidemann RA, Jeje AA, Mohtadi F. *An introduction to the properties of fluids and solids*. Calgary, Canada, University of Calgary Press, 1984.
67. Florence FA, Rushing J, Newsham KE, Blasingame TA. Improved permeability prediction relations for low permeability sands. SPE Rocky Mountain Oil & Gas Technology Symposium, Denver, Colorado, 2007.
68. Wu K, Li X, Wang C, Yu W, Chen Z. Model for surface diffusion of adsorbed gas in nanopores of shale gas reservoirs. *Ind. Eng. Chem. Res.* 2015;54(12):3225-3236.
69. Evans RD, Civan F. Characterization of non-Darcy multiphase flow in petroleum bearing formations. Report, U.S. DOE Contract No. DE-AC22-90BC14659, School of Petroleum and Geological Engineering, University of Oklahoma, 1994.
70. Jones SC. Two-point determinations of permeability and PV vs. net confining stress. *SPE Formation Eval.* 1998;3(1):235-241.
71. Chu L, Ye P, Harmawan IS, Du L, Shepard LR. Characterizing and simulating the nonstationariness and nonlinearity in unconventional oil reservoirs: Bakken application. SPE Canadian Unconventional Resources Conference, Calgary, Alberta, Canada, 2012.

72. Yu W, Sepehrnoori K. Optimization of well spacing for Bakken tight oil reservoirs. SPE/AAPG/SEG Unconventional Resources Technology Conference, Denver, Colorado, 2014b.
73. Chang Y. *Development of a three-dimensional, equation-of-state compositional reservoir simulator for miscible gas flooding*. PhD Dissertation, The University of Texas at Austin, 1990.
74. Lohrenz J, Bray BG, Clark CR. Calculating viscosities of reservoir fluids from their compositions. *J Pet Technol*. 1964;16(10):1171-1176.
75. Peng DY, Robinson DB. A new two-constant equation of state. *Ind Eng Chem Fundam*. 1976;15:59-64.
76. CMG-GEM. *GEM User's Guide*. Computer Modeling Group Ltd, 2012.
77. Wu K, Chen Z, Li J, Li X, Xu J, Dong X. Wettability effect on nanoconfined water flow. *PNAS* 2017;114(13):3358-3363.
78. Wu K, Olson JE. Numerical investigation of complex hydraulic-fracture development in naturally fractured reservoirs. *SPE Prod Oper*. 2016;31(4):300-309.
79. Olson JE, Wu K. Sequential versus simultaneous multi-zone fracturing in horizontal wells: insights from a non-planar, multi-frac numerical model. SPE Hydraulic Fracturing Technology Conference, The Woodlands, Texas, 2012.

**Table 1. Basic parameters used for the simulations**

Parameter	Value	Field Unit	Value	SI Unit
Initial reservoir pressure	4000	psi	27.58	MPa
Reservoir temperature	130	°F	327.59	K
Reservoir thickness	130	ft	39.624	m
Reservoir permeability	800	nD	0.0008	mD
Reservoir porosity	12%	-	12%	-
Initial gas saturation	50%	-	50%	-
Gas gravity	0.58	-	0.58	-
Total compressibility	$3 \times 10^{-6}$	psi <sup>-1</sup>	0.000435	MPa <sup>-1</sup>
Fracture half-length	350	ft	106.68	m
Fracture conductivity	100	md-ft	$3.01 \times 10^{-14}$	m <sup>2</sup> -m
Fracture height	130	ft	39.624	m
Fracture width	0.01	ft	0.003048	m
Fracture spacing	140	ft	42.672	m
Langmuir pressure	1300	psi	8.96	MPa
Langmuir volume	140	scf/ton	3.964	m <sup>3</sup> /ton
Rock density	2.5	g/cm <sup>3</sup>	$2.5 \times 10^3$	kg/m <sup>3</sup>

### Figure captions

**Figure 1.** The relationship between normalized fracture conductivity and closure pressure for three different shale samples: stiff, medium, and soft rock.

**Figure 2.** A basic 3D reservoir model for a horizontal well with 11 planar hydraulic fractures.

**Figure 3.** Different relative permeability curves used for two-phase shale-gas simulation [(a) matrix system; (b) fracture system].

**Figure 4.** Comparison of simulation results of flow rates and cumulative production at a 30-year period between this model and commercial reservoir simulator [(a) gas flow rate and cumulative gas production; (b) water flow rate and cumulative water production].

**Figure 5.** Pressure distribution using this model after 30 years of production.

**Figure 6.** Experimental data of methane desorption at high pressure obeying BET isotherm other than Langmuir isotherm.

**Figure 7.** Effects of gas adsorption and adsorbed gas porosity well performance.

**Figure 8.** Effect of gas slippage and diffusion on well performance with various nanopore sizes between 5 nm to 50 nm.

**Figure 9.** Effects of the combination effects of gas desorption, adsorbed gas porosity, gas slippage and diffusion on well performance.

**Figure 10.** Comparison of pressure distribution after 30 years with and without considering the combining effects of gas desorption, adsorbed gas porosity, and gas slippage and diffusion [(a) with the combining effects; (b) Without the combining effects].

**Figure 11.** Three cases with different natural fracture settings (grey color represents natural fractures) [(a) case 1 with 100 one-set natural fractures; (b) case 2 with 200 one-set

natural fractures; (c) case 3 with 200 two-set natural fractures].

**Figure 12.** Effects of different number and sets of natural fractures on well performance (NF represent natural fracture).

**Figure 13.** Comparison of pressure distribution for different cases after 1000 days and 30 years [(a) base case without NF after 1000 days; (b) base case without NF after 30 years; (c) case 1 after 1000 days; (d) case 1 after 30 years; (e) case 2 after 1000 days; (f) case 2 after 30 years; (g) case 3 after 1000 days; (h) case 3 after 30 years].

**Figure 14.** Distribution of fracture width of generated complex non-planar fracture geometry predicted by the fracture model for a synthetic shale-gas case (grey lines represent natural fractures).

**Figure 15.** Complex non-planar fracture geometry with 100 natural fractures in a synthetic shale-gas case.

**Figure 16.** Pressure-dependent curves of matrix permeability and fracture conductivity used in this study.

**Figure 17.** Effects of pressure-dependent matrix permeability and fracture conductivity on well performance.

**Figure 18.** Comparison of pressure distribution for different scenarios after 1000 days and 30 years [(a) without pressure-dependent effect after 1000 days; (b) without pressure-dependent effect after 30 years; (c) pressure-dependent matrix permeability after 1000 days; (d) pressure-dependent matrix permeability after 30 years; (e) pressure-dependent fracture conductivity after 1000 days; (f) pressure-dependent fracture conductivity after 30 years; (g) pressure-dependent of both after 1000 days; (h) pressure-dependent of both after 30 years].

**Figure 19. Distribution of matrix permeability in the reservoir with complex non-planar fracture geometry and natural fractures.**

**Figure 20. Comparison of well performance between homogeneous and heterogeneous scenarios.**

**Table 1. Basic parameters used for the simulations**



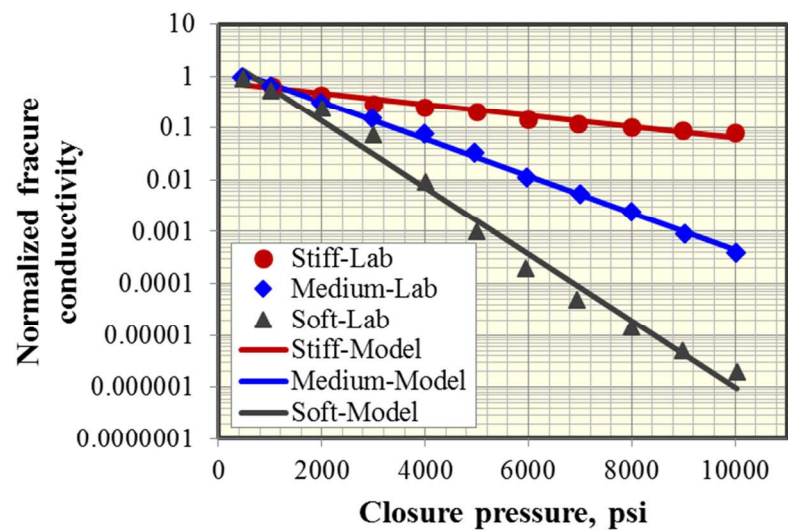


**Figure 1. The relationship between normalized fracture conductivity and closure pressure for three different shale samples: stiff, medium, and soft rock.**

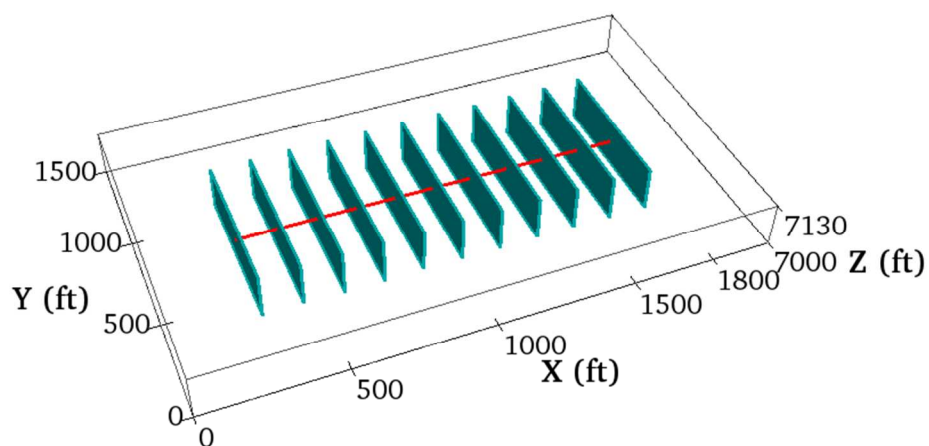


**Figure 2. A basic 3D reservoir model for a horizontal well with 11 planar hydraulic fractures.**

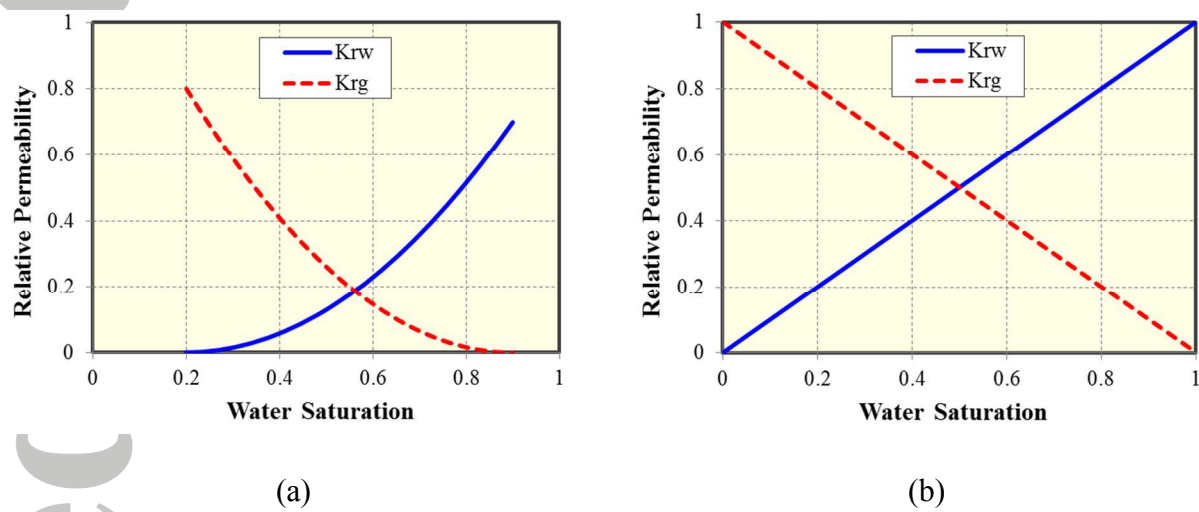
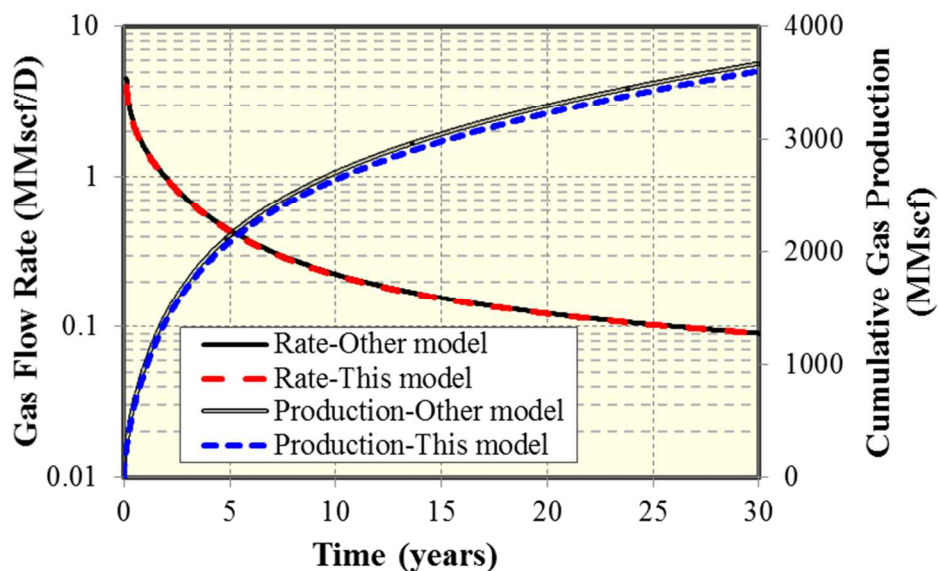
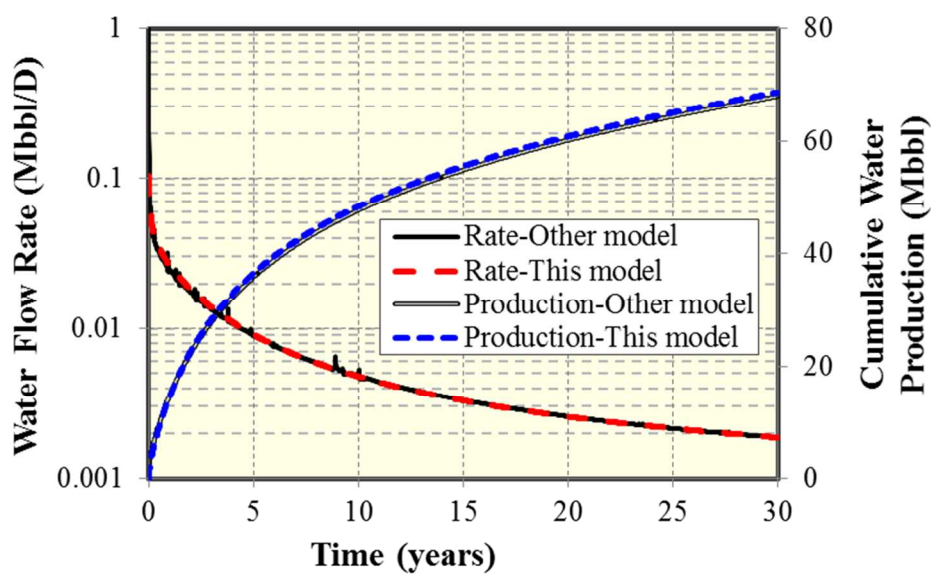


**Figure 3. Different relative permeability curves used for two-phase shale-gas simulation [(a) matrix system; (b) fracture system].**



(a)



(b)

**Figure 4. Comparison of simulation results of flow rates and cumulative production at a 30-year period between this model and commercial reservoir simulator [(a) gas flow rate and cumulative gas production; (b) water flow rate and cumulative water production].**

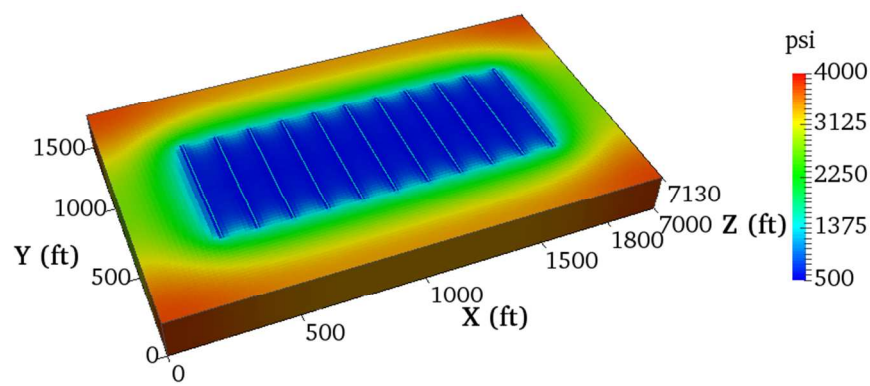


**Figure 5. Pressure distribution using this model after 30 years of production.**

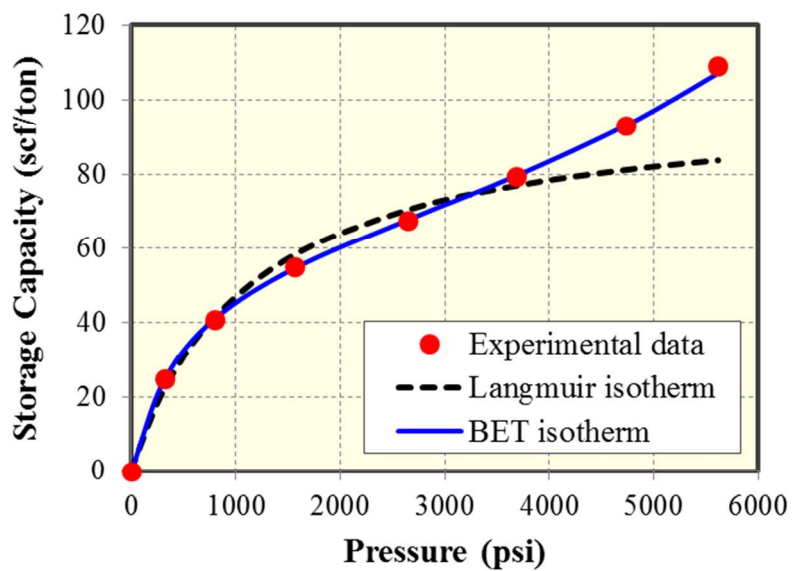


**Figure 6. Experimental data of methane desorption at high pressure obeying BET isotherm other than Langmuir isotherm.**

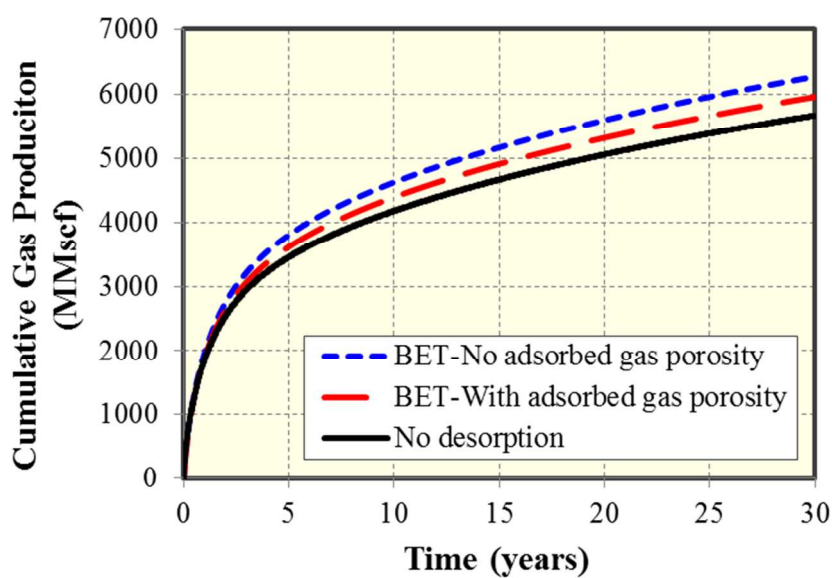
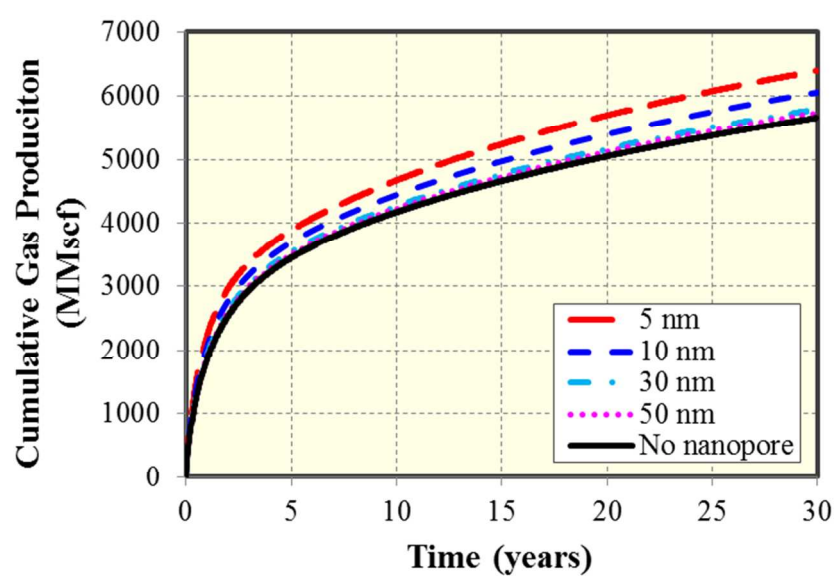
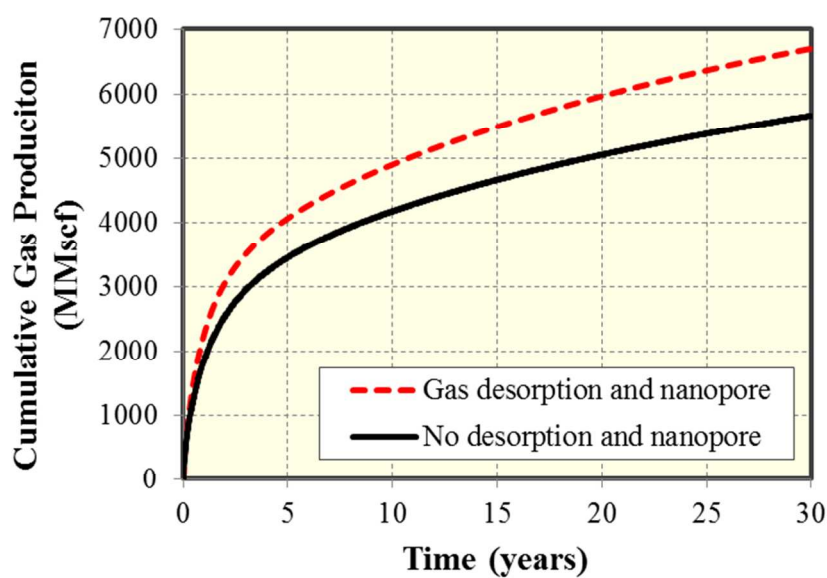


Figure 7. Effects of gas adsorption and adsorbed gas porosity well performance.



**Figure 8. Effect of gas slippage and diffusion on well performance with various nanopore sizes between 5 nm to 50 nm.**





**Figure 9. Effects of the combination effects of gas desorption, adsorbed gas porosity, gas slippage and diffusion on well performance.**

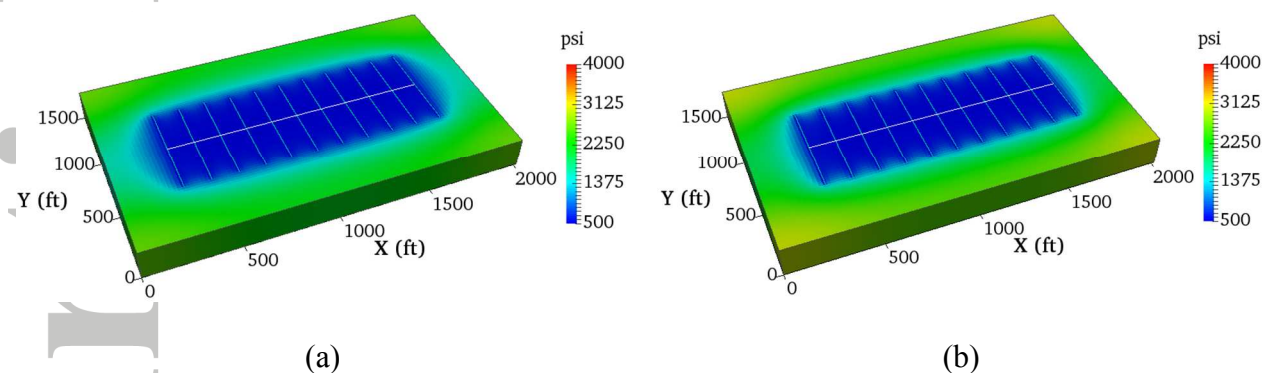
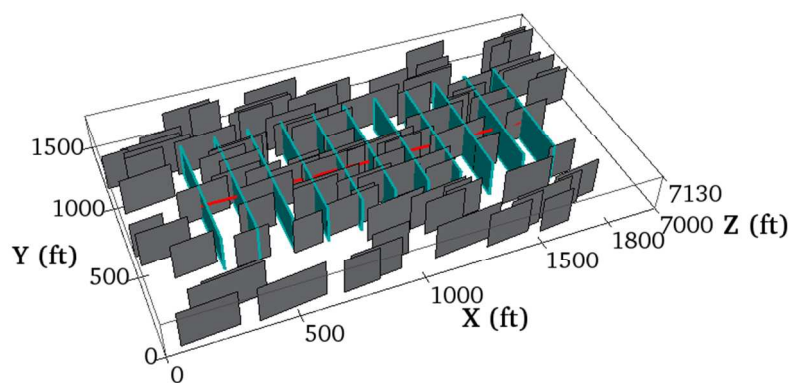
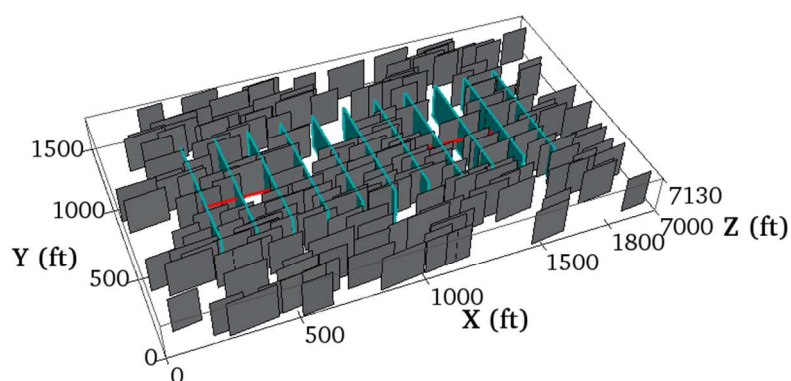


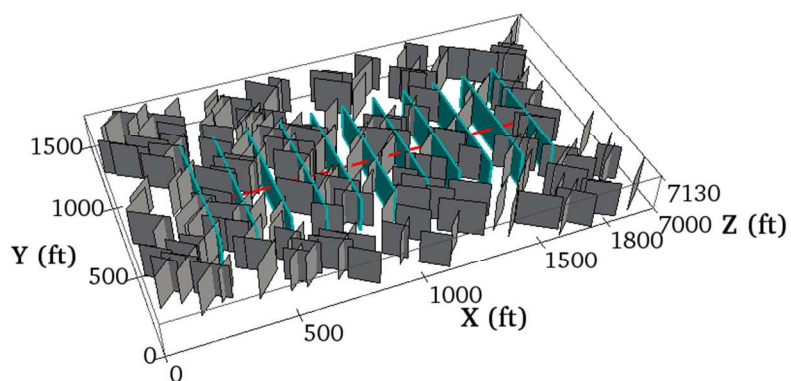
**Figure 10. Comparison of pressure distribution after 30 years with and without considering the combining effects of gas desorption, adsorbed gas porosity, and gas slippage and diffusion [(a) with the combining effects; (b) Without the combining effects].**



(a)



(b)



(c)

**Figure 11. Three cases with different natural fracture settings (grey color represents natural fractures) [(a) case 1 with 100 one-set natural fractures; (b) case 2 with 200 one-set natural fractures; (c) case 3 with 200 two-set natural fractures].**

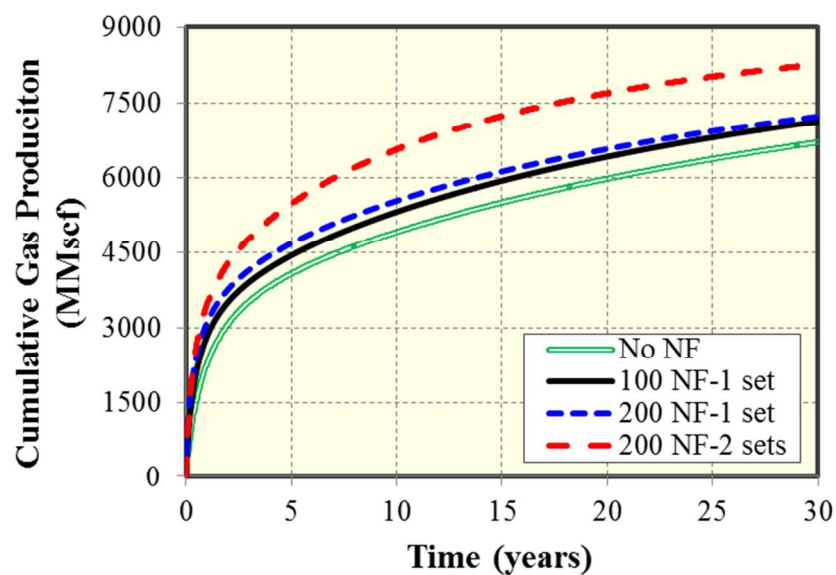


**Figure 12.** Effects of different number and sets of natural fractures on well performance (NF represent natural fracture).

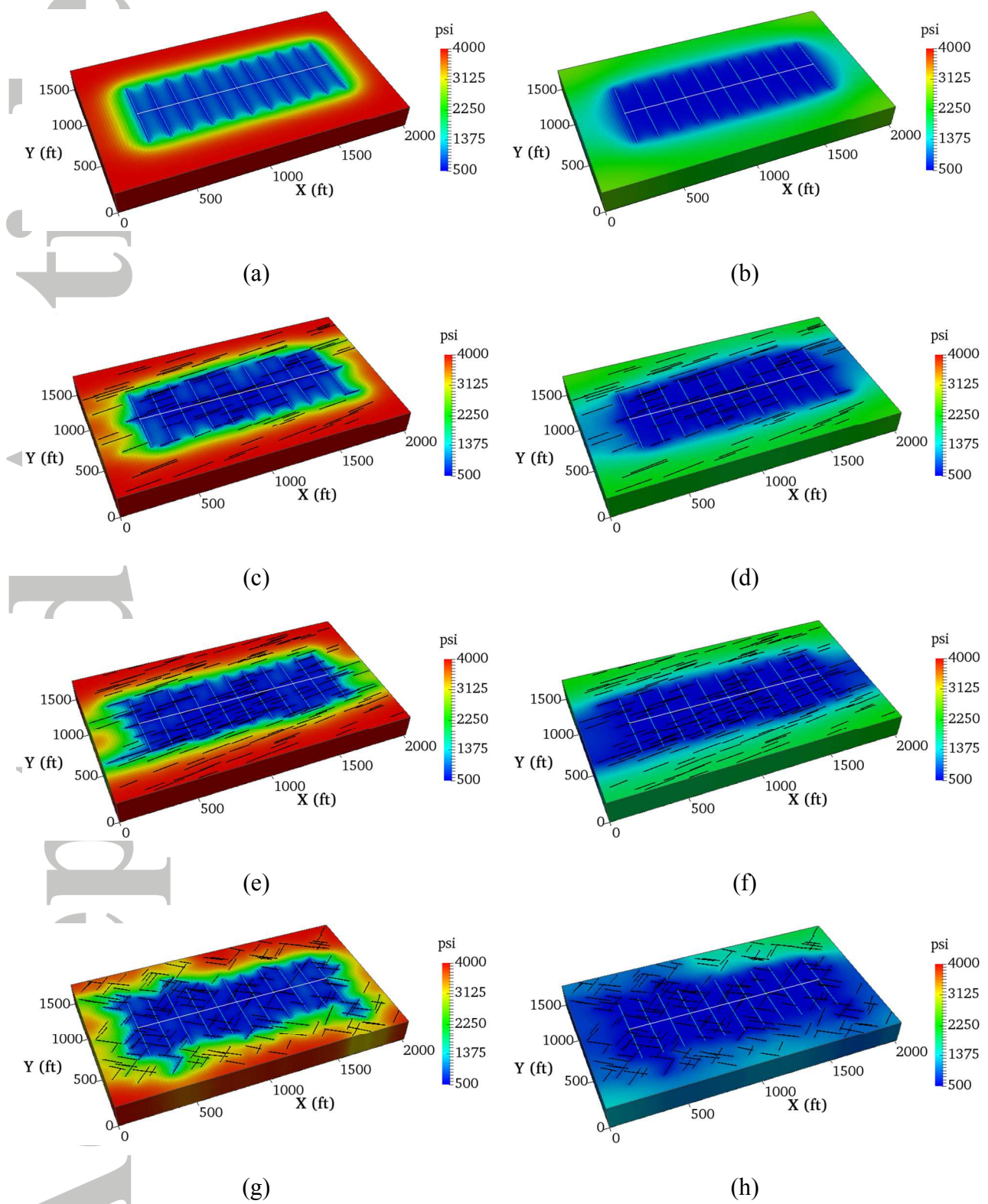


**Figure 13. Comparison of pressure distribution for different cases after 1000 days and 30**

years [(a) base case without NF after 1000 days; (b) base case without NF after 30 years; (c) case 1 after 1000 days; (d) case 1 after 30 years; (e) case 2 after 1000 days; (f) case 2 after 30 years; (g) case 3 after 1000 days; (h) case 3 after 30 years].

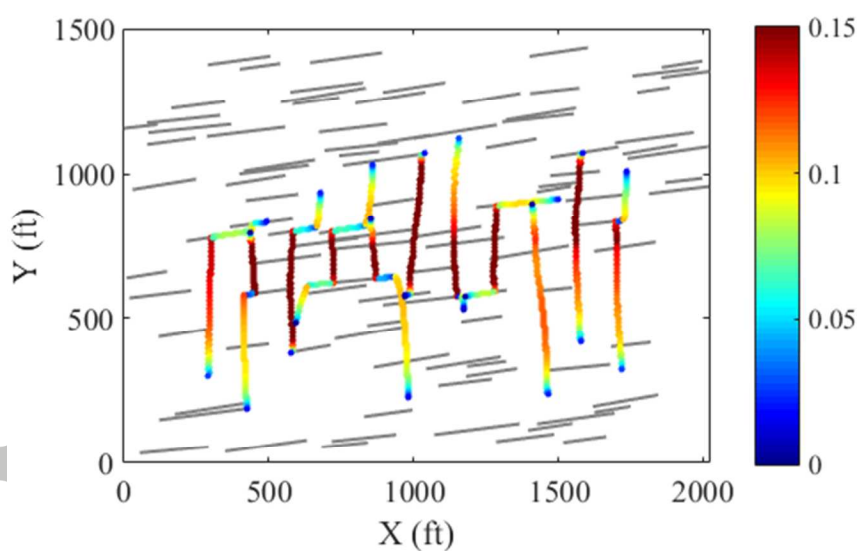


**Figure 14. Distribution of fracture width of generated complex non-planar fracture geometry predicted by the fracture model for a synthetic shale-gas case (grey lines represent natural fractures).**

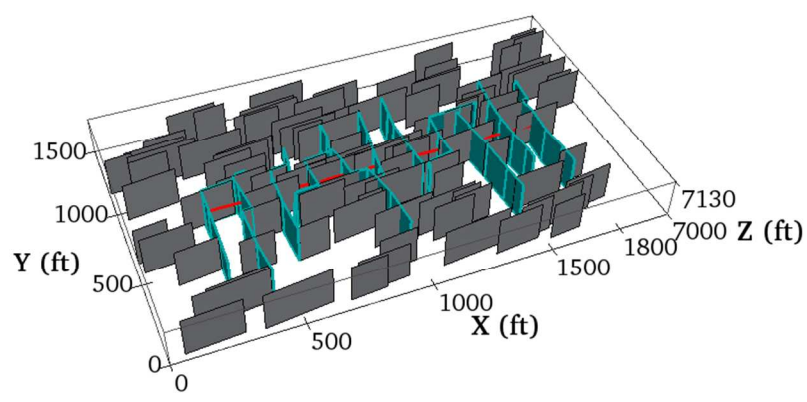


**Figure 15. Complex non-planar fracture geometry with 100 natural fractures in a synthetic shale-gas case.**



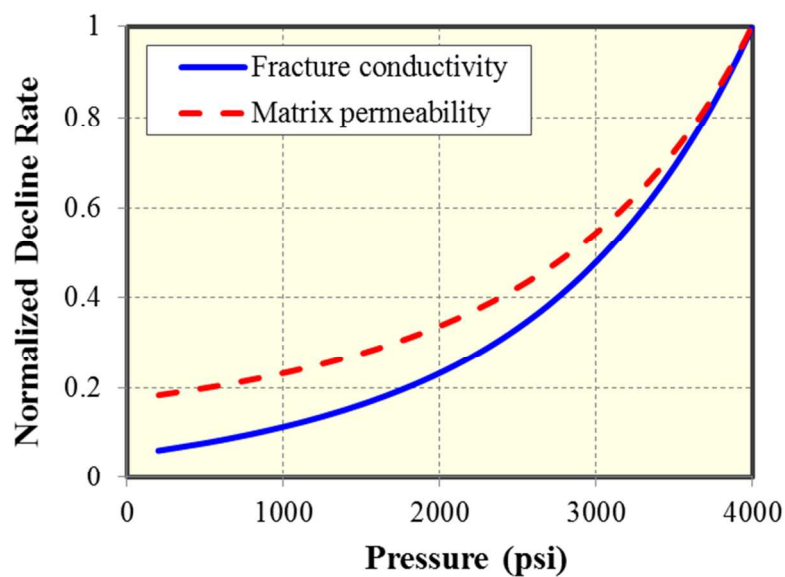


**Figure 16. Pressure-dependent curves of matrix permeability and fracture conductivity used in this study.**



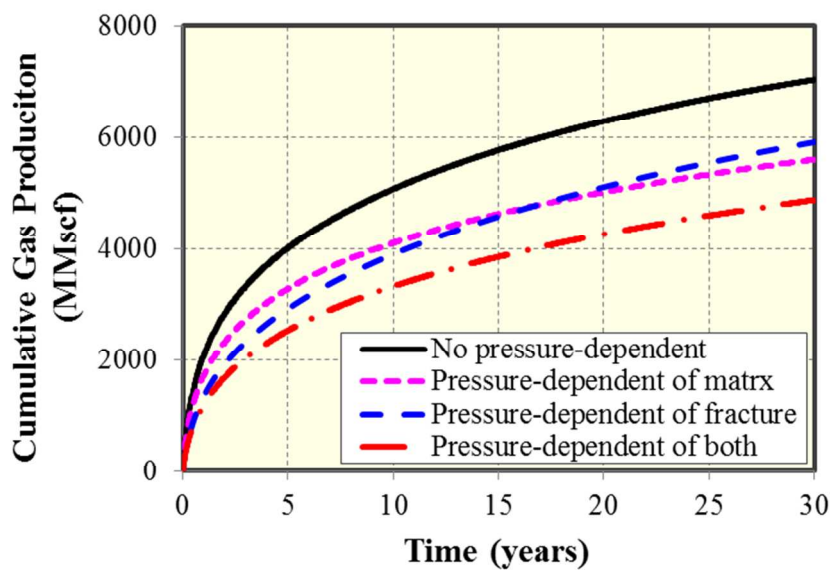


**Figure 17. Effects of pressure-dependent matrix permeability and fracture conductivity on well performance.**

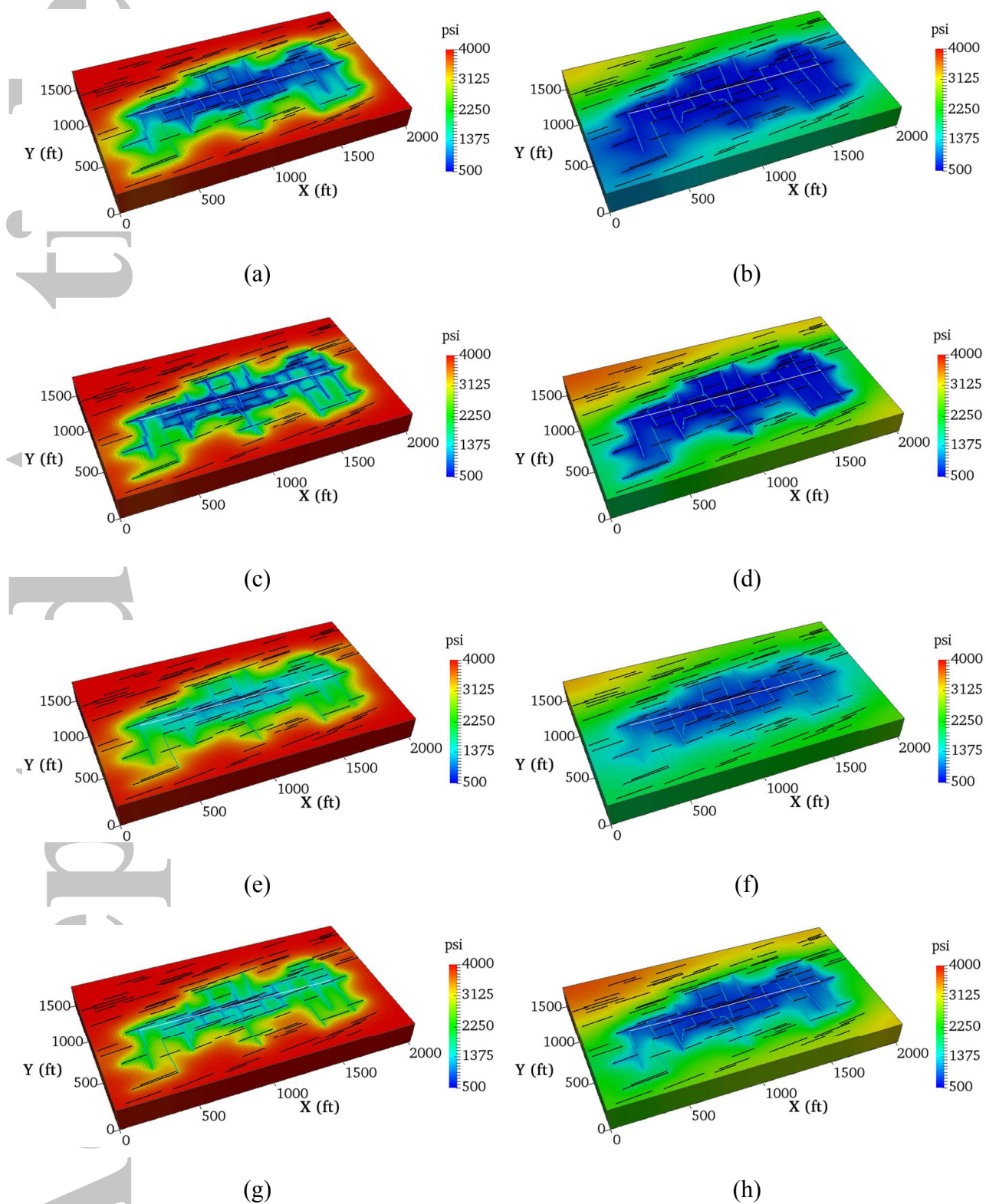


**Figure 18. Comparison of pressure distribution for different scenarios after 1000 days and**

30 years [(a) without pressure-dependent effect after 1000 days; (b) without pressure-dependent effect after 30 years; (c) pressure-dependent matrix permeability after 1000 days; (d) pressure-dependent matrix permeability after 30 years; (e) pressure-dependent fracture conductivity after 1000 days; (f) pressure-dependent fracture conductivity after 30 years; (g) pressure-dependent of both after 1000 days; (h) pressure-dependent of both after 30 years].

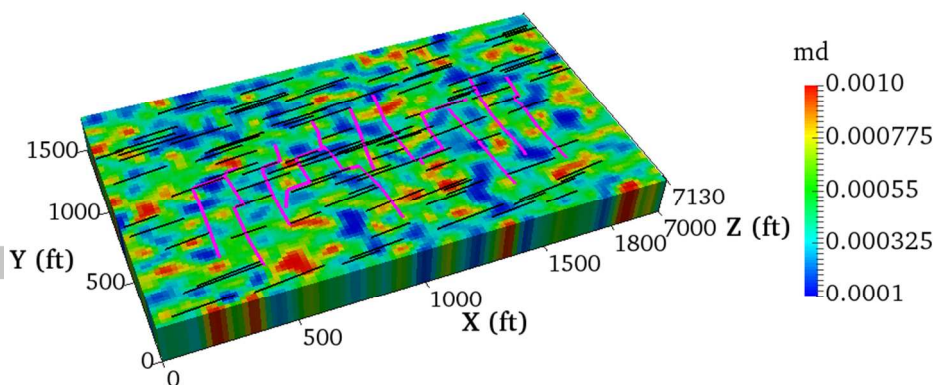


**Figure 19. Distribution of matrix permeability in the reservoir with complex non-planar fracture geometry and natural fractures.**

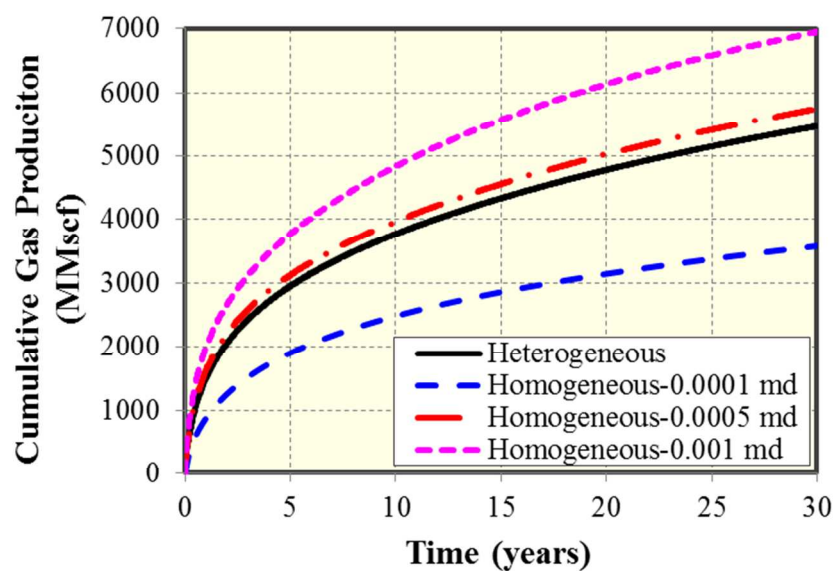


**Figure 20. Comparison of well performance between homogeneous and heterogeneous scenarios.**